



# Fiber taper characterization by optical backscattering reflectometry

YU-HUNG LAI, KI YOUL YANG, MYOUNG-GYUN SUH, AND KERRY J. VAHALA\*

*T. J. Watson Laboratory of Applied Physics, California Institute of Technology, Pasadena, California 91125, USA*

\*[vahala@caltech.edu](mailto:vahala@caltech.edu)

**Abstract:** Fiber tapers provide a way to rapidly measure the spectra of many types of optical microcavities. Proper fabrication of the taper ensures that its width varies sufficiently slowly (adiabatically) along the length of the taper so as to maintain single spatial mode propagation. This is usually accomplished by monitoring the spectral transmission through the taper. In addition to this characterization method it is also helpful to know the taper width versus length. By developing a model of optical backscattering within the fiber taper, it is possible to use backscatter measurements to characterize the taper width versus length. The model uses the concept of a local taper numerical aperture to accurately account for varying backscatter collection along the length of the taper. In addition to taper profile information, the backscatter reflectometry method delineates locations along the taper where fluctuations in fiber core refractive index, cladding refractive index, and taper surface roughness each provide the dominant source of backscattering. Rayleigh backscattering coefficients are also extracted by fitting the data with the model and are consistent with the fiber manufacturer's datasheet. The optical backscattering reflectometer is also used to observe defects resulting from microcracks and surface contamination. All of this information can be obtained before the taper is removed from its fabrication apparatus. The backscattering method should also be prove useful for characterization of nanofibers.

© 2017 Optical Society of America

**OCIS codes:** (060.2270) Fiber characterization; (140.3945) Microcavities; (290.1350) Backscattering.

## References and links

1. K. J. Vahala, "Optical microcavities," *Nature* **424**(6950), 839–846 (2003).
2. A. B. Matsko and V. S. Ilchenko, "Optical resonators with whispering gallery modes I: Basics," *IEEE J. Sel. Top. Quant. Electron.* **12**(1), 3–14 (2006).
3. T. J. Kippenberg, R. Holzwarth and S. A. Diddams, "Microresonator-based optical frequency combs," *Science* **332**(6029), 555–559 (2011).
4. P. Del'Haye, A. Schliesser, O. Arcizet, T. Wilken, R. Holzwarth and T. J. Kippenberg, "Optical frequency comb generation from a monolithic microresonator," *Nature* **450**(7173), 1214–1217 (2007).
5. T. Herr, V. Brasch, J. D. Jost, C. Y. Wang, N. M. Kondratiev, M. L. Gorodetsky and T. J. Kippenberg, "Temporal solitons in optical microresonators," *Nat. Photon.* **8**(2), 145–152 (2014).
6. V. Brasch, M. Geiselmann, T. Herr, G. Lihachev, M. H. P. Pfeiffer, M. L. Gorodetsky and T. J. Kippenberg, "Photonic chip-based optical frequency comb using soliton Cherenkov radiation," *Science* **351**(6271), 357–360 (2016).
7. X. Yi, Q. F. Yang, K. Y. Yang, M. G. Suh and K. J. Vahala, "Soliton frequency comb at microwave rates in a high-Q silica microresonator," *Optica* **2**(12), 1078–1085 (2015).
8. S. M. Spillane, T. J. Kippenberg and K. J. Vahala, "Ultralow-threshold Raman laser using a spherical dielectric microcavity," *Nature* **415**(6872), 621–623 (2002).
9. M. Tomes and T. Carmon, "Photonic micro-electromechanical systems vibrating at X-band (11-GHz) rates," *Phys. Rev. Lett.* **102**(11), 113601 (2009).
10. I. S. Grudin, A. B. Matsko and L. Maleki, "Brillouin lasing with a CaF<sub>2</sub> whispering gallery mode resonator," *Phys. Rev. Lett.* **102**(4), 043902 (2009).
11. J. Li, H. Lee and K. J. Vahala, "Microwave synthesizer using an on-chip Brillouin oscillator," *Nat. Commun.* **4**, 2097 (2013).
12. T. Carmon and K. J. Vahala, "Visible continuous emission from a silica microphotonic device by third-harmonic generation," *Nat. Phys.* **3**(6), 430–435 (2007).
13. B. J. Eggleton, C. G. Poulton and R. Pant, "Inducing and harnessing stimulated Brillouin scattering in photonic integrated circuits," *Adv. Opt. Photon.* **5**(4), 536–587 (2013).

14. G. Bahl, M. Tomes, F. Marquardt and T. Carmon, "Observation of spontaneous Brillouin cooling," *Nat. Phys.* **8**(3), 203–207 (2012).
15. T. J. Kippenberg and K. J. Vahala, "Cavity optomechanics: back-action at the mesoscale," *Science* **321**(5893), 1172–1176 (2008).
16. M. Eichenfield, J. Chan, R. Camacho, K. J. Vahala and O. Painter, "Optomechanical crystals," *Nature* **462**(7269), 78–82 (2009).
17. I. S. Grudin, H. Lee, O. Painter and K. J. Vahala, "Phonon laser action in a tunable two-level system," *Phys. Rev. Lett.* **104**(8), 083901 (2010).
18. J. Chan, T. P. Mayer Alegre, A. H. Safavi-Naeini, J. T. Hill, A. Krause, S. Gröblacher, M. Aspelmeyer and O. Painter, "Laser cooling of a nanomechanical oscillator into its quantum ground state," *Nature* **478**(7367), 89–92 (2011).
19. F. Monifi, J. Zhang, Ş. K. Özdemir, B. Peng, Y. X. Liu, F. Bo, F. Nori and L. Yang, "Optomechanically induced stochastic resonance and chaos transfer between optical fields," *Nat. Photon.* **10**(6), 399–405 (2016).
20. B. Peng, Ş. K. Özdemir, S. Rotter, H. Yilmaz, M. Liertzer, F. Monifi, C. M. Bender, F. Nori and L. Yang, "Loss-induced suppression and revival of lasing," *Science* **346**(6207) 328–332 (2014).
21. L. Del Bino, J. M. Silver, S. L. Stebbings and P. Del'Haye, "Symmetry Breaking of Counter-Propagating Light in a Nonlinear Resonator," *Sci. Rep.* **7**, 43142 (2017).
22. T. Aoki, B. Dayan, E. Wilcut, W. P. Bowen, A. S. Parkins, T. J. Kippenberg, K. J. Vahala and H. J. Kimble, "Observation of strong coupling between one atom and a monolithic microresonator," *Nature* **443**(7112), 671–674 (2006).
23. K. Srinivasan and O. Painter, "Linear and nonlinear optical spectroscopy of a strongly coupled microdisk-quantum dot system," *Nature* **450**(7171), 862–865 (2007).
24. F. Vollmer and S. Arnold, "Whispering-gallery-mode biosensing: label-free detection down to single molecules," *Nat. Methods*, **5**(7), 591–596 (2008).
25. F. Vollmer and L. Yang, "Label-free detection with high-Q microcavities: a review of biosensing mechanisms for integrated devices," *Nanophotonics* **1**(3-4), 267–291 (2012).
26. J. Zhu, S. K. Ozdemir, Y. F. Xiao, L. Li, L. He, D. R. Chen and L. Yang, "On-chip single nanoparticle detection and sizing by mode splitting in an ultrahigh-Q microresonator," *Nat. Photon.* **4**(1), 46–49 (2010).
27. T. Lu, H. Lee, T. Chen, S. Herchak, J.-H. Kim, S. E. Fraser, R. C. Flagan, and K. J. Vahala, "High sensitivity nanoparticle detection using optical microcavities," *Proc. Natl. Acad. Sci.* **108**, 5976–5979 (2011).
28. J. Li, M. G. Suh and K. J. Vahala, "Microresonator Brillouin gyroscope," *Optica* **4**(3), 346–348 (2017).
29. W. Liang, V. S. Ilchenko, A. A. Savchenkov, E. Dale, D. Eliyahu, A. B. Matsko and L. Maleki, "Resonant microphotonic gyroscope," *Optica* **4**(1), 114–117 (2017).
30. J. Alnis, A. Schliesser, C. Y. Wang, J. Hofer, T. J. Kippenberg and T. W. Hänsch, "Thermal-noise-limited crystalline whispering-gallery-mode resonator for laser stabilization," *Phys. Rev. A* **84**(1), 011804 (2011).
31. H. Lee, M. G. Suh, T. Chen, J. Li, S. A. Diddams and K. J. Vahala, "Spiral resonators for on-chip laser frequency stabilization," *Nat. Commun.* **4**, 2468 (2013).
32. W. Loh, A. A. Green, F. N. Baynes, D. C. Cole, F. J. Quinlan, H. Lee, K. J. Vahala, S. B. Papp and S. A. Diddams, "Dual-microcavity narrow-linewidth Brillouin laser," *Optica* **2**(3), 225–232 (2015).
33. J. C. Knight, G. Cheung, F. Jacques and T. A. Birks, "Phase-matched excitation of whispering-gallery-mode resonances by a fiber taper," *Opt. Lett.* **22**(15), 1129–1131 (1997).
34. M. Cai, O. Painter and K. J. Vahala, "Observation of critical coupling in a fiber taper to a silica-microsphere whispering-gallery mode system," *Phys. Rev. Lett.* **85**(1), 74 (2000).
35. S. M. Spillane, T. J. Kippenberg, O. J. Painter and K. J. Vahala, "Ideality in a fiber-taper-coupled microresonator system for application to cavity quantum electrodynamics," *Phys. Rev. Lett.* **91**(4), 043902 (2003).
36. E. Vetsch, D. Reitz, G. Sagué, R. Schmidt, S. T. Dawkins and A. Rauschenbeutel, "Optical interface created by laser-cooled atoms trapped in the evanescent field surrounding an optical nanofiber," *Phys. Rev. Lett.* **104**(20), 203603 (2010).
37. A. Goban, K. S. Choi, D. J. Alton, D. Ding, C. Lacroûte, M. Pototschnig, T. Thiele, N. P. Stern and H. J. Kimble, "Demonstration of a state-insensitive, compensated nanofiber trap," *Phys. Rev. Lett.* **109**(3), 033603 (2012).
38. T. A. Birks, W. J. Wadsworth and P. S. J. Russell, "Supercontinuum generation in tapered fibers," *Opt. Lett.* **25**(19), 1415–1417 (2000).
39. W. J. Wadsworth, A. Ortigosa-Blanch, J. C. Knight, T. A. Birks, T. P. M. Man and P. S. J. Russell, "Supercontinuum generation in photonic crystal fibers and optical fiber tapers: a novel light source," *J. Opt. Soc. Am. B* **19**(9), 2148–2155 (2002).
40. P. Lu, L. Men, K. Sooley and Q. Chen, "Tapered fiber Mach-Zehnder interferometer for simultaneous measurement of refractive index and temperature," *Appl. Phys. Lett.* **94**(13), 131110 (2009).
41. O. Frazão, P. Caldas, F. M. Araújo, L. A. Ferreira and J. L. Santos, "Optical flowmeter using a modal interferometer based on a single nonadiabatic fiber taper," *Opt. Lett.* **32**(14), 1974–1976 (2007).
42. D. J. Alton, "Interacting single atoms with nanophotonics for chip-integrated quantum networks," PhD thesis, California Institute of Technology, Chap. 7 (2013).
43. L. Ding, C. Belacel, S. Ducci, G. Leo and I. Favero, "Ultralow loss single-mode silica tapers manufactured by a microheater," *Appl. Opt.* **49**(13), 2441–2445 (2010).
44. A. W. Snyder and J. D. Love, *Optical waveguide theory* (Chapman and Hall, London, 1983).

45. T. A. Birks and Y. W. Li, "The shape of fiber tapers," *J. Lightwave Tech.* **10**(4), 432–438 (1992).
46. A. H. Hartog and M. P. Gold, "On the theory of backscattering in single-mode optical fibers," *J. Lightwave Tech.* **2**(2), 76–82 (1984).
47. M. Nakazawa, "Rayleigh backscattering theory for single-mode optical fibers," *J. Opt. Soc. Am.* **73**(9), 1175–1180 (1983).
48. B. J. Soller, D. K. Gifford, M. S. Wolfe and M. E. Froggatt, "High resolution optical frequency domain reflectometry for characterization of components and assemblies," *Opt. Express* **13**(2), 666–674 (2005).
49. U. Glombitza and E. Brinkmeyer, "Coherent frequency-domain reflectometry for characterization of single-mode integrated-optical waveguides," *J. Lightwave Tech.* **11**(8), 1377–1384 (1993).
50. H. Barfuss and E. Brinkmeyer, "Modified optical frequency domain reflectometry with high spatial resolution for components of integrated optic systems," *J. Lightwave Tech.* **7**(1), 3–10, (1989).
51. W. Eickhoff and R. Ulrich, "Optical frequency domain reflectometry in single-mode fiber," *Appl. Phys. Lett.* **39**(9), 693–695 (1981).
52. M. E. Lines, "Scattering losses in optic fiber materials, I. A new parametrization, II. Numerical estimates," *J. Appl. Phys.* **55**(11), 4052–4063 (1984).
53. K. Tsujikawa, K. Tajima and J. Zhou, "Intrinsic loss of optical fibers," *Opt. Fiber Tech.* **11**(4), 319–331 (2005).
54. M. Ohashi, K. Shiraki and K. Tajima, "Optical loss property of silica-based single-mode fibers," *J. Lightwave Tech.* **10**(5), 539–543 (1992).
55. A. Yariv, *Electronics in modern communications, 5th Ed.* (Oxford University, 1997), Chap. 3.
56. M. Borselli, T. Johnson and O. Painter, "Beyond the Rayleigh scattering limit in high-Q silicon microdisks: theory and experiment," *Opt. Express* **13**(5), 1515–1530 (2005).
57. M. L. Gorodetsky, A. D. Pryamikov and V. S. Ilchenko, "Rayleigh scattering in high-Q microspheres," *J. Opt. Soc. Am. B* **17**(6), 1051–1057 (2000).
58. K. Saito, M. Yamaguchi, H. Kakiuchida, A. J. Ikushima, K. Ohsono and Y. Kurosawa, "Limit of the Rayleigh scattering loss in silica fiber," *Appl. Phys. Lett.* **83**(25), 5175–5177 (2003).
59. S. Sakaguchi and S. Todoroki, "Rayleigh scattering of silica core optical fiber after heat treatment," *Appl. Opt.* **37**(33), 7708–7711 (1998).
60. G. P. Agrawal, *Nonlinear Fiber Optics, 4th Ed.* (Academic Press, 2006).

## 1. Introduction

Over the last decade a remarkably wide range of new research areas and applications have emerged that rely upon high-quality-factor optical microcavities [1, 2]. These include frequency microcombs [3, 4] including soliton mode-locked microcombs [5–7], nonlinear parametric and stimulated oscillators [8–11], harmonic generation [12], Brillouin signal processing [13] and cooling [14], cavity optomechanics [15–19], studies of physical symmetry [20, 21], cavity quantum electrodynamics [22, 23], sensing [24–27], optical gyroscopes [28, 29], and reference cavities [30–32]. Rapid prototyping and testing of both discrete and monolithic resonators in the laboratory frequently make use of fiber tapers for optical coupling [33–35]. Beyond rapid testing, this method provides controllable loading of the resonator by variation of a coupling air gap [34], which is often essential to understand performance optimization. Tapers are also intrinsically fiber compatible so that their interface with pump lasers, detectors and spectrometers is straightforward. Outside of their use in microresonator research, fiber tapers and the closely-related optical nanofiber are applied to trap atoms [36, 37], for supercontinuum generation [38, 39], and in sensing applications [40, 41]. The methods developed here should also prove useful in these applications.

A properly fabricated fiber taper can readily achieve both critical and over-coupled operation with high ideality [34, 35, 42, 43]. Ideal tapers have two key features. First, they are nearly single mode near the region at which optical coupling to the resonator will occur. Second, they maintain propagation in a single spatial mode as the fiber profile is reduced from a width of 125 microns (for SMF-28 fiber) to a width of around 1 micron. This latter adiabatic condition requires that the taper width varies slowly along its length [44, 45]. The adiabatic condition can be tested by measuring coupling ideality [35] or monitoring the spectral transmission through the taper [34, 43].

This work studies the application of optical backscatter reflectometry (OBR) to characterize the width versus length of fiber tapers. Instead of using an optical microscope (limited spatial

resolution) or a scanning electron microscope (potential taper damage risk) for point-wise profile examination, it is shown that modeling combined with the OBR data can extract the taper profile with good accuracy (within 20% of the width profile obtained by measurement using an SEM). The OBR data also provide information on imperfections along the taper. Significantly, the method is nondestructive and can be applied while the taper is within its fabrication assembly. It is therefore useful when developing a taper pulling schedule, when using a new fiber type for taper fabrication, in verifying taper pulling reproducibility and for identification of defects and contamination. It is possible to discern distinct regions where the optical mode propagates primarily within the fiber core, the fiber cladding and finally the taper waist region. Rayleigh scattering coefficients are also extracted using the backscattering model [46, 47] and the inferred values are consistent with the scattering coefficients of the fibers.

In the following sections, example OBR measurements are presented and compared with the corresponding taper width versus length profiles obtained by scanning electron microscopy. The model used to infer taper profile information from backscatter data is then developed. Finally, the model is applied in combination with OBR data to study several tapers.

## 2. Taper fabrication and measurement

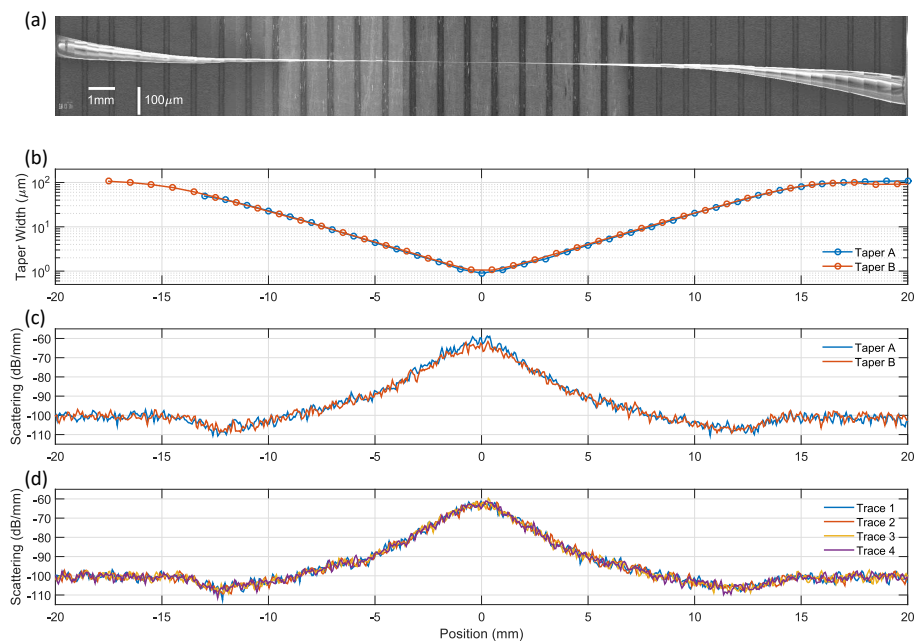


Fig. 1. Taper width versus position measurement and OBR measurement. (a) A composite image is presented for a fiber taper. The image was produced by stitching together a series of scanning electron microscope (SEM) images as described in the text. The black vertical lines in the image are 1 mm tick marks on a metal ruler and provide a reference used to construct the image. The scale factors for the vertical and horizontal axes are different and are provided in the legend. (b) Width versus position profiles measured on two different tapers are presented. The tapers were fabricated under the same conditions and measured using the SEM method in panel (a). (c) OBR data for the two tapers in panel (b). The consistency between taper profiles and scattering traces verifies the reproducibility of the fabrication system. (d) Four sets of OBR data taken using one taper illustrate the consistency of the OBR measurement.

To fabricate a taper, the plastic jacket is removed along a section of SMF-28 fiber and the two ends of the exposed glass fiber are attached to fiber holders in a chuck. The holders are free to slide under the control of motorized translation stages. The exposed fiber is heated with a ceramic microheater and the motorized stages gradually pull the fiber at a speed of approximately 0.2 millimeters per second. The taper waist width is adjusted by either changing the pulling length or by varying the temperature of the microheater. After fabrication, the taper is left in its fabrication apparatus and backscatter characterization is performed at room temperature.

A scanning electron microscope (SEM) is used to image the taper profile as shown in Fig. 1(a). The image is a composite of a series of scans. The vertical and horizontal scales in the image are different (see scale bars in legend). To construct the image, a fiber taper is mounted on a metal ruler with 1 mm tick spacings. The ruler then functions as a reference to combine the SEM images together. Using such images recorded for two tapers, width versus position plots were constructed in Fig. 1(b). The plots closely match and verify the reproducibility of the taper fabrication system. The vertical scale is logarithmic and also shows that (away from the taper waist region) the taper width varies exponentially over a wide range of the taper length. This behavior is expected on account of a well defined softened region of glass produced by the heater [43]. The narrow region of the taper has a length of only a few millimeters in the present work. However, the backscatter method should also be able to characterize structures having longer waist regions.

Backscatter reflectometry was performed using a LUNA OBR 4400. This instrument measures backscatter strength versus position using the frequency domain method. Optical frequency domain reflectometry uses swept-frequency coherent interferometry to measure a device under test [48–51]. In the instrument the laser center wavelength is nominally 1566 nm and the laser sweeping bandwidth is 88 nm. The highest spatial resolution setting along the propagation direction is 10 microns. OBR sweep signals are presented in Fig. 1(c) measured using the two tapers from Fig. 1(b). The signals show a high level of consistency. In addition, four OBR sweep traces performed on a single taper are shown in Fig. 1(d) to verify the repeatability of the OBR measurement.

### 3. Backscatter signal model

Refractive-index fluctuations in the glass [52–54] and surface-roughness scattering in the taper waist region are the dominant sources of scattering. The resulting backscattered light must be collected by the fiber waveguide so as to be guided to the OBR instrument. The collection efficiency for this process has been analyzed for single-mode optical fiber [46] and depends upon the local mode field diameter. Fiber waveguides with smaller mode field diameters are more efficient in collecting the backscattered light, because they have a larger numerical aperture. The taper adiabaticity condition makes it possible to introduce a local backscatter collection efficiency (effectively, there is a local numerical aperture). The collection efficiency results originally developed for standard optical fiber can then be applied to a fiber taper where the mode field diameter is slowly varying.

To further explore the backscattering process, the simulated intensity profile of an  $HE_{11}$  mode [55] along a taper is provided in Fig. 2. Comparing the profile with the measured backscatter data in Fig. 1(c), the initial backscatter level in Fig. 1(c) is determined by the refractive index fluctuations of the SMF-28 fiber core region. As the core tapers down in width, there is an initial reduction in the backscattering level that accompanies the expansion of the optical mode into the surrounding glass cladding region. This reduction is expected on account of the reduced optical backscattering collection efficiency with increasing mode field diameter (i.e., reduced local numerical aperture). Then, when the taper width is less than 50 microns, increasing confinement provided by the glass-air interface boosts the backscattering collection efficiency. Since the mode field now extends well outside of the fiber core, the backscattering

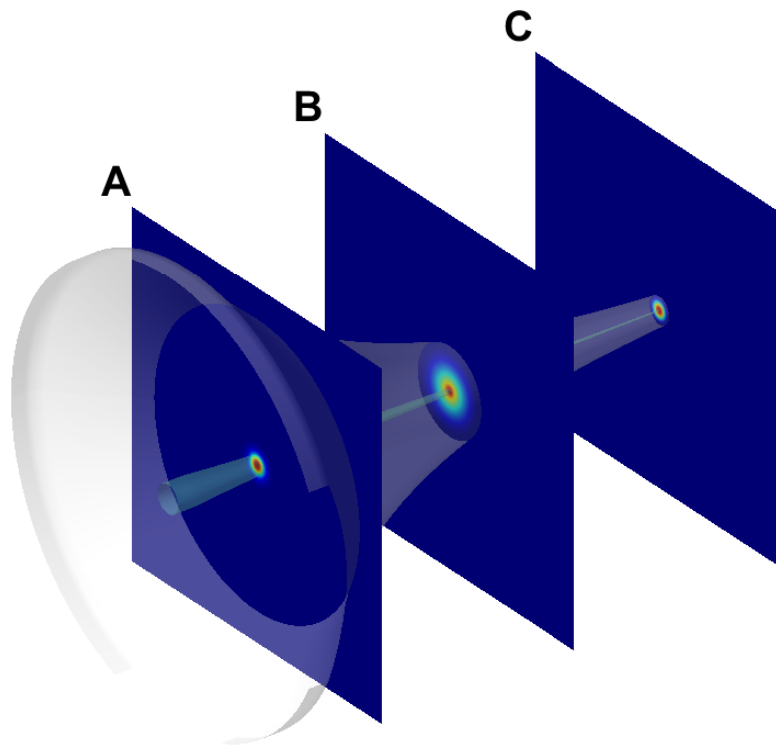


Fig. 2. Illustration showing a fiber taper with a  $HE_{11}$  mode profile superimposed. The blue planes give the energy density profiles associated with the transverse polarization. Initially in region A, light is confined in the core region and the fluctuations in refractive index of the core dominate the scattering process. In region B, the taper width is reduced to tens of microns and a substantial portion of the optical power is propagating within the cladding region. Here, the refractive-index fluctuations of the cladding dominate the scattering process. Region C occurs around the taper waist where the surrounding air functions as the cladding and the taper surface roughness dominates the scattering process.

signal in this region is dominated by refractive index fluctuations within the fiber cladding. Finally, when the taper width is around 3-4 microns the glass-air interface scattering becomes dominant. Despite the relatively small cross-sectional area presented by surface roughness fluctuations in comparison to the cladding density fluctuations, the large difference in the refractive index of air and dielectric increases the strength of the surface scattering [56,57]. To connect backscattering power to taper width versus position, it is in principle possible to construct a look-up table based on taper calibrations. However, a model of backscattering has several advantages over such an empirical method. First, the model provides a physical understanding of the behavior observed in the taper backscattering signal. Second, it provides quantitative values for Rayleigh scattering coefficients associated with core, cladding and surface scattering. Finally, these Rayleigh coefficients provide reference data that serve to monitor the taper fabrication process over time (e.g., surface smoothness of the waist region).

The above physical picture of scattering motivates a model for normalized backscatter power per unit length. The contributions to backscattering from the core, cladding and taper surface are described by three terms in Eq. (1) below. Details on the derivation are provided in the Appendix.

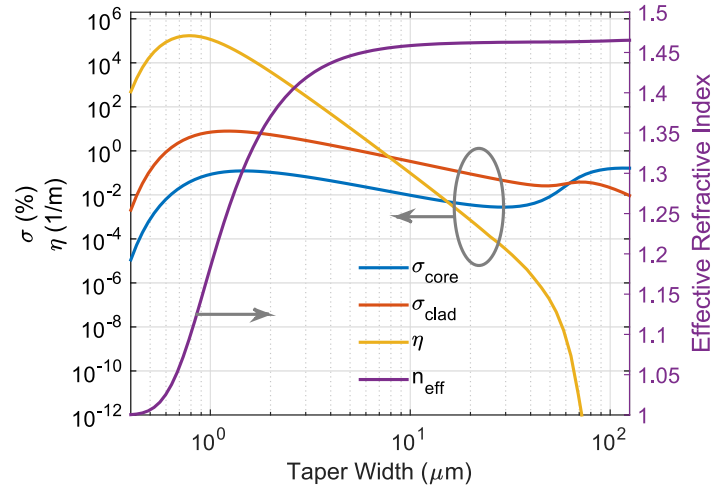


Fig. 3. Calculation of the parameters  $\sigma_{\text{core}}$ ,  $\sigma_{\text{clad}}$  and  $\eta$  in Eq. (1) versus the taper width  $w$ . The calculations used a finite element method solver. The effective index,  $n_{\text{eff}}$ , is also presented. For the narrowest taper widths  $n_{\text{eff}}$  approaches unity, the index of air, while at the largest widths it has the index of the SMF-28 fiber used to prepare the fiber taper. The wavelength assumed is 1566 nm and SMF-28 parameters are:  $w_{\text{clad}} = 125\mu\text{m}$ ,  $w_{\text{core}} = 8.2\mu\text{m}$ ,  $n_{\text{core}} = 1.4682$ ,  $n_{\text{clad}} = 1.4631$ .

$$\frac{1}{P_{\text{in}}} \frac{dP_{\text{OBR}}(w(z))}{dz} = \alpha_{\text{core}} \sigma_{\text{core}}(w(z)) + \alpha_{\text{clad}} \sigma_{\text{clad}}(w(z)) + \beta \eta(w(z)) \quad (1)$$

where  $P_{\text{in}}$  is the total input power to the taper and  $dP_{\text{OBR}}(w(z))/dz$  is the backscattered power per unit length at taper position  $z$  with  $w(z)$  the width of the taper at position  $z$ .  $\alpha_{\text{core}}$  and  $\alpha_{\text{clad}}$  are the Rayleigh scattering coefficients in the core and cladding regions, respectively.  $\beta$  is the Rayleigh surface scattering coefficient at the taper-air interface (see Appendix). These parameters are determined by fitting to the OBR data.  $\sigma_{\text{core}}$  and  $\sigma_{\text{clad}}$  are related to backscattering contributions in the core and in the cladding respectively.  $\eta$  is related to backscattering contributions at the taper glass-air interface. These parameters account for cross sectional variations of the core, cladding and surface as well as the local coupling efficiency of the scattered light into the taper guided mode. Their forms follow from the analysis for backscattering in standard optical fiber [46]:

$$\sigma_{\text{core,clad}} \equiv \frac{3\lambda^2}{8\pi n^2} \frac{\int_{\text{core,clad}} |\vec{E}(\vec{r})|^4 dS}{\left( \int_{\text{all}} |\vec{E}(\vec{r})|^2 dS \right)^2} \quad (2)$$

$$\eta \equiv \frac{3\lambda^2}{8\pi n^2} \frac{\oint_{\text{interface}} |\vec{E}(\vec{r})|^4 dl}{\left( \int_{\text{all}} |\vec{E}(\vec{r})|^2 dS \right)^2} \quad (3)$$

where each integration is performed at a specific width  $w(z)$  along the fiber taper.  $\lambda$  is the center wavelength of the OBR laser scan, and  $n$  is the fiber refractive index (small differences in core and cladding regions are neglected). The analysis leading to these forms is provided in the Appendix. A key assumption made in the analysis is that powers from distinct, random scatterers are added to compute the total scattered power. This is equivalent to assuming that the correlation length for scattering centers is much smaller than the optical wavelength. A finite element solver is used to calculate  $\sigma_{\text{core}}$ ,  $\sigma_{\text{clad}}$  and  $\eta$  as a function of the taper width,  $w$ . The results are shown in Fig. 3.

Because, as noted above, the backscatter signal is generated using a wavelength sweep over 88 nm centered at 1566 nm, it is important to check the wavelength dependence of the parameters in Fig. 3. It is found that there is a negligible variation in their values relative to the scale of signal variations in the measurement.

In the analysis, it is assumed that the taper maintains a circular cross section and that the ratio of core width to taper width is constant along the taper. Moreover, the statistical properties of the scatterers within the core and cladding regions are assumed to be uniform in each region. Also, scattering centers at the glass-air interface are assumed to be spatially uniform in their statistical properties. These assumptions mean that  $\alpha_{\text{core}}$ ,  $\alpha_{\text{clad}}$  and  $\beta$  are treated as constants and, based on the analysis [46,47], are expected to be intensive quantities. Finally, an additional assumption is that the attenuation of the input power along the length of the taper is so weak that the propagating power along the length of the fiber taper can be treated as constant.

An additional effect must be added to the model on account of the effective index variation along the length of the fiber taper as its width varies. In performing a conversion of time delay into distance, the OBR system assumes that the effective index is a constant over the length of the optical fiber (in this case SMF-28). However, since the effective refractive index decreases as taper width decreases, light propagates faster within the taper region and this causes the OBR to detect the signal earlier and thereby incorrectly compute a scattering location too close to the OBR instrument. Accordingly, a location  $z_{\text{OBR}}$  given by the following equation is computed by the instrument,

$$\int_0^z n_{\text{eff}}(w(z')) dz' = n_{\text{OBR}} z_{\text{OBR}} \quad (4)$$

where  $n_{\text{eff}}(w(z))$  is the taper effective index at location  $z$  and  $n_{\text{OBR}}$  is the effective index assumed by the OBR instrument. Given a taper profile  $w(z)$  and using the  $n_{\text{eff}}(w)$  from Fig. 3, it is possible to convert  $z$  into  $z_{\text{OBR}}$  ( $z \rightarrow z_{\text{OBR}}$ ) using the above equation. Also, because the OBR signal is a relative scattering per unit length in  $z_{\text{OBR}}$  units, the form of the left hand side of Eq. (1) in units measured by the OBR instrument is the following:

$$\frac{dP_{\text{OBR}}}{dz} = \frac{dP_{\text{OBR}}}{dz_{\text{OBR}}} \frac{dz_{\text{OBR}}}{dz} = n_{\text{corr}}(w) \frac{dP_{\text{OBR}}}{dz_{\text{OBR}}} \quad (5)$$

where the corrected refractive index factor is defined as,

$$n_{\text{corr}}(w) = \frac{n_{\text{eff}}(w)}{n_{\text{OBR}}} \quad (6)$$

Therefore, in calculating the instrument measured OBR signal, both the position correction provided by Eq. (4) and the scaling correction of Eq. (1) given in Eq. (5) must be used.

Eqs. (1)-(6) allow three distinct calculations to be performed that are illustrated schematically in the Fig. 4 flow charts.

*Calculation I* [blue arrows in Fig. 4(a)]: This calculation computes the  $(\alpha_{\text{core}}, \alpha_{\text{clad}}, \beta)$  scattering coefficients. A taper profile is measured ( $w(z)$ ) and used to calculate  $n_{\text{eff}}$ ,  $\sigma_{\text{core}}$ ,  $\sigma_{\text{clad}}$  and  $\eta$  as a function of  $z$  by applying results in Fig. 3. These results are used to map  $z$  into  $z_{\text{OBR}}$  using Eq. (4). Equation (1) (in the measured  $z_{\text{OBR}}$ -units provided by Eq. (5)) is then fit to the experimental backscatter data. The result of this fitting is a set of  $(\alpha_{\text{core}}, \alpha_{\text{clad}}, \beta)$  constants. To ensure consistent values for  $(\alpha_{\text{core}}, \alpha_{\text{clad}}, \beta)$  the fiber type used to fabricate the taper should not be varied. Also, although the taper profile can be varied, such things as the annealing schedule and furnace temperature should be maintained constant so as to ensure similar density fluctuations in the glass [58,59].

*Calculation II* [orange arrows in Fig. 4(a)]: This calculation uses a measured taper profile and existing  $(\alpha_{\text{core}}, \alpha_{\text{clad}}, \beta)$  coefficients to predict an OBR trace for a given taper. A taper profile is

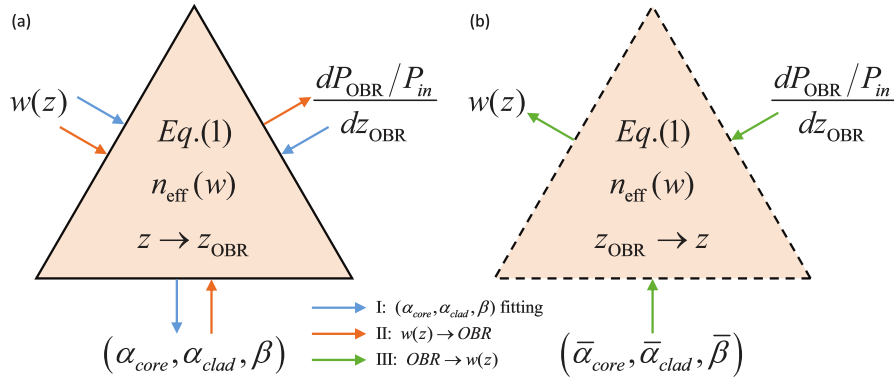


Fig. 4. Flow charts illustrating three distinct taper-related calculations that are possible. (a) Calculation I (blue): a known taper profile is combined with OBR data to determine fitting parameters  $(\alpha_{core}, \alpha_{clad}, \beta)$ . Calculation II (orange): a known taper profile is combined with average fitting parameters  $(\bar{\alpha}_{core}, \bar{\alpha}_{clad}, \bar{\beta})$  to predict an OBR signal. (b) Calculation III: an OBR signal is combined with average fitting parameters  $(\bar{\alpha}_{core}, \bar{\alpha}_{clad}, \bar{\beta})$  to determine a taper profile. This particular measurement is performed in a piecewise fashion on regions where the OBR signal monotonically varies with taper length.

first measured  $w(z)$  and used to calculate  $n_{eff}$ ,  $\sigma_{core}$ ,  $\sigma_{clad}$  and  $\eta$  as a function of  $z$  by applying the results in Fig. 3. Conversion of  $z \rightarrow z_{OBR}$  is performed as in Calculation I. These results are then combined with the existing  $(\alpha_{core}, \alpha_{clad}, \beta)$  constants to predict an optical backscatter signal using Eq. (1). Averaged constants  $(\bar{\alpha}_{core}, \bar{\alpha}_{clad}, \bar{\beta})$  obtained by measuring several tapers can be used to improve accuracy.

*Calculation III* [green arrows in Fig. 4(b)]: A third calculation is to determine an unknown taper profile,  $w(z)$ , from OBR data and averaged scattering coefficients  $(\bar{\alpha}_{core}, \bar{\alpha}_{clad}, \bar{\beta})$  obtained using other tapers having different profiles. Because the taper width is not a one-to-one function of the OBR signal as shown in Fig. 1(b) and Fig. 1(c), it is convenient to perform this calculation in a piecewise fashion within specific taper regions where the OBR signal varies monotonically with length. A taper whose profile  $w(z)$  is to be determined is characterized to obtain its OBR signal versus  $z_{OBR}$ . When restricted to the piecewise regions noted above, each OBR data point maps uniquely into a  $w$  value using Eq. (1) (corrected using the scaling in Eq. (5)) in conjunction with Fig. 3. This establishes the function  $w(z_{OBR})$  since the OBR instrument provides the OBR signal versus  $z_{OBR}$ . Using Eq. (4), it follows,

$$\frac{dz_{OBR}}{dz} = n_{corr}(w(z_{OBR})) \quad (7)$$

from which the conversion of OBR position to actual position ( $z_{OBR} \rightarrow z$ ) can be computed as the following integral,

$$z = \int_0^{z_{OBR}} \frac{dz'_{OBR}}{n_{corr}(w(z'_{OBR}))} \quad (8)$$

This, in turn, allows  $w(z_{OBR})$  to be converted into the actual taper profile  $w(z)$ . For tapers having widths  $< 800\text{nm}$ , the taper waist region must be separated in the piecewise analysis since the OBR signal once again becomes multi-valued (see  $\sigma_{core}$ ,  $\sigma_{clad}$  and  $\eta$  curves in Fig. 3).

Table 1. Rayleigh Scattering Coefficients of Different SMF-28 Tapers Pulled at 1660°C

Taper Number	Waist Width ( $\mu\text{m}$ )	$\alpha_{\text{core}}$ ( $10^{-6}/\text{m}$ )	$\alpha_{\text{clad}}$ ( $10^{-6}/\text{m}$ )	$\beta$ ( $10^{-9}$ )
1a	0.49	45.2	81.3	4.39
2a	0.90	51.2	75.0	3.69
3a	1.02	40.9	87.1	3.94
4a	1.05	37.1	90.8	3.46
5a	1.34	49.2	95.2	3.47
6a	1.74	45.5	67.4	4.85
Average		$45 \pm 5$ (11%)	$83 \pm 10$ (12%)	$4.0 \pm 0.6$ (15%)

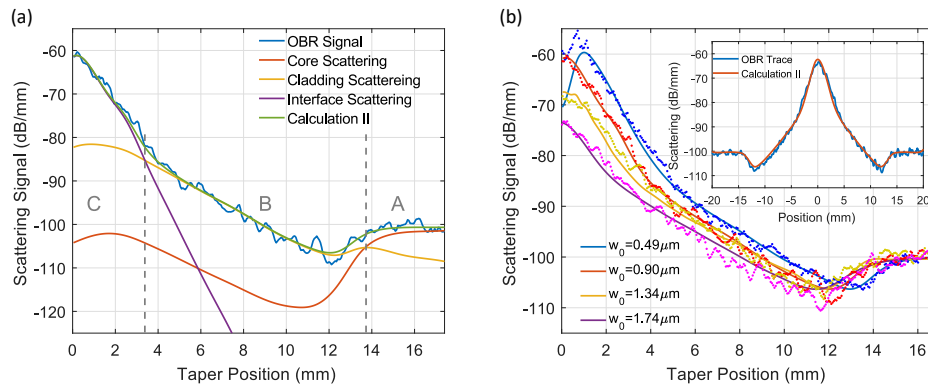


Fig. 5. Predicted OBR signal is compared with actual OBR data. (a) OBR data from taper 2a in Table 1 is plotted versus taper position relative to the taper waist at one end of the taper. The data are compared with the prediction based on Calculation II using the average parameters in Table 1. Also shown are the contributions from the three scattering mechanisms in Eq. (1). A, B, and C intervals delineated by the dashed vertical lines (see Fig. 2) give regions in which each mechanism provides the dominant contribution to total scattering. (b) Averaged parameters from measurements on the 6 tapers in Table 1 are used to predict the OBR signal measurements (dots) from four tapers (Table I) by using Calculation II (solid curves). Taper waist widths are provided in the legend. Note that for the smallest taper width,  $0.49 \mu\text{m}$ , the model successfully predicts the reduction in the OBR scattering at the taper waist qualitatively. Inset: OBR trace over the full length of taper 4a is compared with the prediction using Calculation II.

#### 4. Determination of taper Rayleigh scattering coefficients ( $\alpha_{\text{core}}$ , $\alpha_{\text{clad}}$ , $\beta$ )

The coefficients ( $\alpha_{\text{core}}$ ,  $\alpha_{\text{clad}}$ ,  $\beta$ ) provide information on refractive index fluctuations in the core, cladding and interface regions. The coefficients can in principle depend upon the oven temperature and annealing applied during taper fabrication. Assuming that oven temperature and annealing are not varied, it should not be necessary to remeasure these parameters. In a first test, six tapers were prepared using SMF-28 optical fiber by pulling at 1660°C. The oven temperature was inferred from the manufacturer datasheet and drive current. A range of waist widths was intentionally produced by adjusting the pulling distance for each taper. OBR data was first measured for each taper. After this, the taper profiles,  $w(z)$ , were measured using an SEM as described in Fig. 1. A weighted-least-squares fitting of Eq. (1) (corrected to  $z_{\text{OBR}}$  units) to the OBR data is then performed to extract ( $\alpha_{\text{core}}$ ,  $\alpha_{\text{clad}}$ ,  $\beta$ ) for each taper using Calculation I. The fitting results are provided in Table 1.

## 5. Determination of the optical backscatter signal from $w(z)$

As a test of the Calculation II method to predict OBR signals from a set of parameters, the averaged fitting parameters are calculated in the last row of Table 1 and used to compute the backscatter signal from Eq. (1) for four tapers (1a, 2a, 5a and 6a in Table 1). The computed results for a single taper are shown in Fig. 5(a). The separate contributions to the overall scattering power from the three underlying contributions are also plotted. In Fig. 5(b), the computed results for the four tapers are presented. The agreement between the predicted OBR signal and the measured signal is reasonable. It is interesting to note that the reduction in the backscatter signal at the waist of the narrowest taper is correctly predicted by the model using the single set of averaged fitting parameters. For the narrowest waist width measured, the glass-air interface scattering drops around this region because of increased propagation in the air.

$z_{\text{OBR}}$  is plotted versus  $z$  in Fig. 6(a) to illustrate the impact of the varying effective index on the scattering location as inferred by the OBR instrument. The maximum OBR position error (difference between propagation in tapered and untapered fiber) ranges from 0.13 mm ( $w_0 = 1.74\mu\text{m}$ ) to 0.57 mm ( $w_0 = 0.49\mu\text{m}$ ) after only 2 mm of light propagation.

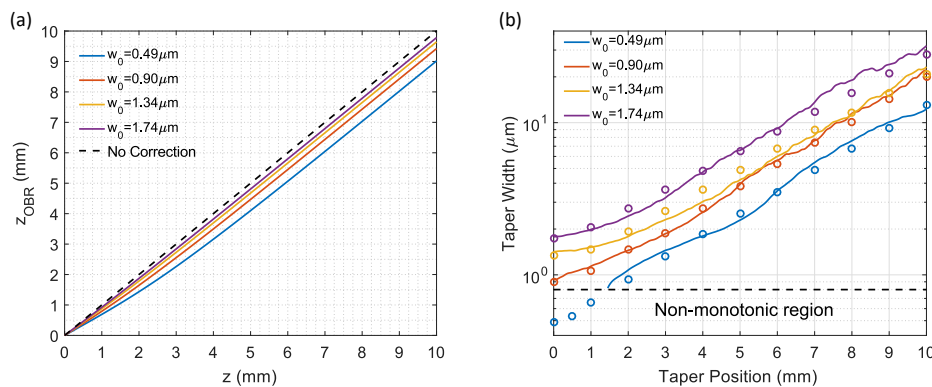


Fig. 6. (a) The position  $z_{\text{OBR}}$  calculated from Eq. (4) plotted versus position  $z$  for tapers 1a, 2a, 5a, 6a in Table 1. Zero on both axes corresponds to the taper center. The calculated OBR position error ranges from 0.13 mm ( $w_0 = 1.74\mu\text{m}$ ) to 0.57 mm ( $w_0 = 0.49\mu\text{m}$ ) after 2 mm of light propagation and is caused by the varying effective index along the taper. The legend gives the taper waist width and the black dashed line is the case  $z_{\text{OBR}} = z$ . (b) The taper width versus position as determined from the OBR signal using Calculation III is plotted for four tapers from Table I (solid curves). The circles are the taper profiles measured using an SEM. The taper waist widths are provided in the legend.

## 6. Determination of $w(z)$ from the optical backscatter signal

To determine the width versus position profile from the OBR signal trace, the OBR traces are numerically smoothed before analysis to reduce fluctuations. Using the Calculation III procedure, the taper width versus taper position profiles calculated for four of the tapers in Table 1 are presented in Fig. 6(b). While the entire taper could be analyzed, the results are presented for one side of the taper. The inferred taper profiles approximately follow an exponential variation with length. For comparison, the SEM measured profiles of the four tapers are included as the circles. The agreement is good. The relative deviation between the taper profile estimated by OBR and that measured by an SEM is within 20%. A summary of the minimum taper waist widths as inferred from the OBR measurement and the directly measured waist widths using the SEM is provided in Table 2. Note that one taper is thin enough ( $0.49\mu\text{m}$ ) to exhibit non-monotonic OBR

behavior near the taper center. Nonetheless, the taper profile is estimated correctly outside this region.

Table 2. Waist Width Comparison of Tapers Pulled at 1660°C

SEM Measurement ( $\mu\text{m}$ )	OBR Estimation ( $\mu\text{m}$ )	Relative Deviation
0.90	0.93	+3.3%
1.34	1.42	+6.0%
1.74	1.77	+1.7%

## 7. Variation of fiber type and pulling temperature

To study the effect of pulling temperature and fiber type on these procedures, three additional SMF-28 fiber tapers were prepared but with the oven temperature set to 1550°C. Also, three SM980 fiber tapers were prepared at this oven temperature. OBR and SEM measurements were performed and calculation I in Fig. 4 was applied to determine the new Rayleigh coefficients ( $\alpha_{\text{core}}$ ,  $\alpha_{\text{clad}}$ ,  $\beta$ ) shown in Table 3 (note: an SM980 calculation corresponding to Fig. 3 for SMF-28 was also performed using SM980 fiber parameters:  $w_{\text{clad}} = 125\mu\text{m}$ ,  $w_{\text{core}} = 5.7\mu\text{m}$ ,  $n_{\text{core}} = 1.4499$ ,  $n_{\text{clad}} = 1.4440$ ). Comparing results for the SMF-28 fiber in Table 1 and Table 3, the coefficient  $\bar{\alpha}_{\text{core}}$  is similar in value. On the other hand, when the pulling temperature is lower the parameter  $\bar{\alpha}_{\text{clad}}$  decreases about 40% and  $\bar{\beta}$  decreases about 20%, suggesting that the lower temperature pulling reduced the refractive-index fluctuations and surface scattering in the taper. On the other hand, the values of the SMF-28 and SM980 coefficients  $\bar{\alpha}_{\text{core}}$ ,  $\bar{\alpha}_{\text{clad}}$  and  $\bar{\beta}$  in Table 3 for tapers pulled at the same temperature are within the range of the experimental deviation. This is reasonable since the core and cladding compositions of the two fiber types are germanium-doped silica and pure silica, respectively. Their scattering properties should therefore be similar.

Table 3. Rayleigh Scattering Coefficients of Different Taper Types Pulled at 1550°C

SMF-28				
Taper Number	Waist Width ( $\mu\text{m}$ )	$\alpha_{\text{core}}$ ( $10^{-6}/\text{m}$ )	$\alpha_{\text{clad}}$ ( $10^{-6}/\text{m}$ )	$\beta$ ( $10^{-9}$ )
1b	0.90	54.7	56.0	3.38
2b	1.25	39.0	49.1	2.96
3b	1.76	48.6	42.2	2.81
Average		$48 \pm 8$ (17%)	$49 \pm 7$ (14%)	$3.0 \pm 0.3$ (10%)
SM980				
Taper Number	Waist Width ( $\mu\text{m}$ )	$\alpha_{\text{core}}$ ( $10^{-6}/\text{m}$ )	$\alpha_{\text{clad}}$ ( $10^{-6}/\text{m}$ )	$\beta$ ( $10^{-9}$ )
1c	1.37	42.7	52.4	3.18
2c	1.62	36.9	54.3	2.90
3c	2.56	54.7	49.4	3.99
Average		$45 \pm 9$ (20%)	$52 \pm 3$ (6%)	$3.4 \pm 0.6$ (18%)

As a further test, the average coefficients ( $\bar{\alpha}_{\text{core}}$ ,  $\bar{\alpha}_{\text{clad}}$ ,  $\bar{\beta}$ ) were used to determine the backscattering signals of these fibers (Calculation II). Also, Calculation III was applied to determine  $w(z)$ . The results are presented in Fig. 7 with comparison to measurements. The relative deviation

between the SEM measured and the OBR predicted taper profiles in Fig. 7(b) and 7(d) is within 15%. It is interesting to note that the exponential profile observable in the tapers fabricated at higher temperature is not observed in the tapers fabricated at the lower temperature.

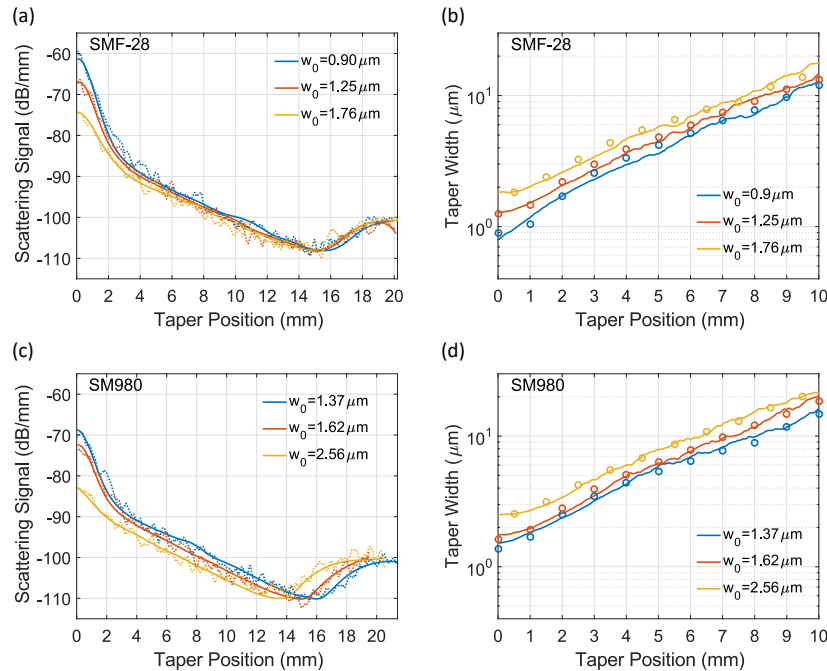


Fig. 7. Measured and predicted OBR signals and taper profiles for SMF-28 and SM980 tapers pulled at 1550°C. (a) SMF-28 OBR signal traces (dots) and the Calculation II prediction (solid curve). (b) SMF-28 profiles measured by an SEM (circles) and profiles predicted using Calculation III (solid curves). (c) SM980 OBR signal traces (dots) and the Calculation II prediction (solid curve). (d) SM980 profiles measured by an SEM (circles) and profiles predicted using Calculation III (solid curves). Taper waist widths are given in the legend of each panel.

## 8. Other OBR taper measurements

It is interesting to compare the inferred Rayleigh scattering coefficients for the core and cladding regions of the taper with those computed for the core region of the original (unpulled) optical fiber. Also, because the dominant loss mechanism is expected to be scattering at the wavelengths measured, it is possible to infer a Rayleigh scattering parameter by using the fiber manufacturer's specified attenuation coefficient. This comparison is made in Table 4 and results are in fairly close agreement. Here, the Rayleigh coefficient is written as  $\alpha'$  in dB/km attenuation units where  $\alpha'(\text{dB/km}) = 10^4(\log_{10} e)\alpha(1/\text{m})$  [52] and  $\alpha$  is the mks-units form in Eq. (1).

Beyond using the OBR analysis to predict the taper profile or to use a taper profile to predict OBR signals, the backscattering method also provides diagnostic information on taper defects such as might be caused by dust or micro-cracks. As one example, two back-scattering traces are recorded using a dusty taper by recording the OBR signal from opposite ends of the taper. The OBR traces in Fig. 8(a) contain scattering features that mirror one another indicating the presence of the dust particles. As another example, Fig. 8(b) presents scans of a taper both before and after

Table 4. Taper Rayleigh Scattering Coefficients Comparison With Optical Fiber

Fiber Type (Temp.)	SMF-28 (1660°C)	SMF-28 (1550°C)	SM980 (1550°C)
$\alpha'_{\text{core}}$ (dB/km)	$0.20 \pm 0.02$	$0.21 \pm 0.03$	$0.20 \pm 0.04$
$\alpha'_{\text{clad}}$ (dB/km)	$0.36 \pm 0.04$	$0.21 \pm 0.03$	$0.23 \pm 0.01$
OBR Meas. (dB/km)	$0.26 \pm 0.01$	$0.23 \pm 0.01$	$0.28 \pm 0.01$
Data Sheet (dB/km)	0.25	0.25	n.a.*

\*Not provided by manufacturer.

appearance of what is believed to be a microcrack. The microcrack formed under application of tension to the taper and is accompanied by appearance of a spike-like feature near the backscatter maximum. As further evidence of the microcrack, a bright scattering point is observed near the center of the taper when a white LED is shining on the taper region.

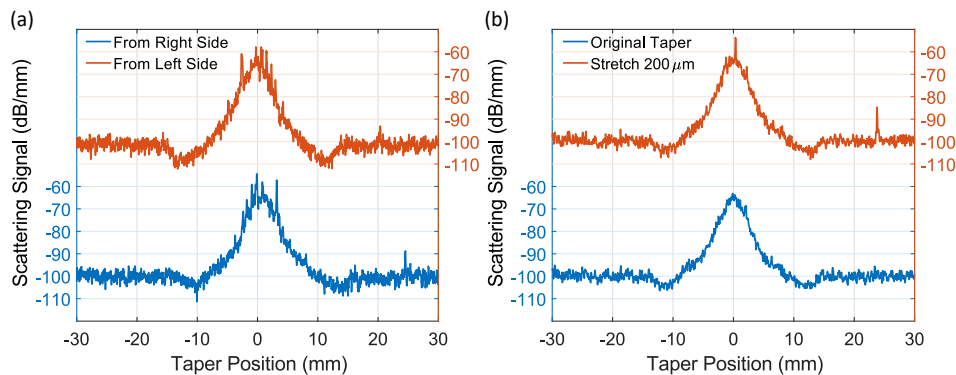


Fig. 8. OBR measurements of dust and microcracks. (a) Backscatter traces produced by coupling into the right and left ends of a taper are shown. Evidence of dust or defects on the taper appear as small spikes in the backscatter signal and, as expected, switch sides in the traces relative to the taper center. (b) Lower trace shows an OBR trace without tension. Upper trace shows the scan when tension is increased to induce what is believed to be a microcrack.

## 9. Conclusion

When combined with modeling, optical backscatter reflectometry provides a way to characterize the width versus position profile of an optical fiber taper. The OBR signal, itself, also measures the mode evolution from fiber core to taper waveguiding as it propagates through the taper. The model developed to fit the data accounts for scattering mechanisms associated with the fiber core and cladding of the bulk silica glass as well as surface scattering along the narrow portions of the taper. It also includes the variation of backscatter coupling into the taper guided mode on account of the varying taper width. Rayleigh scattering coefficients for core, cladding and taper surface were extracted by fitting the model with the OBR data. The experimentally determined Rayleigh backscattering coefficients for the core and cladding are consistent with those inferred from attenuation data in the fiber manufacturer's datasheet. The OBR method of taper characterization is nondestructive and can be performed while the taper is within its fabrication system. Moreover, it can be used to measure defects and contamination. The method also provides a convenient way to calibrate a taper pulling recipe. The OBR characterization method developed here could be applied to analyze width variations in chip-integrated waveguides.

## Appendix

For convenience, a short derivation of Eq. (1) is provided in this section based on the analysis in ref [47]. The taper-guided mode  $\vec{E}_n(\vec{r})$  induces a polarization  $\vec{P} = \Delta\epsilon(\vec{r})\vec{E}_n = 2\epsilon_o n \Delta n(\vec{r})\vec{E}_n$  (and a displacement current  $\vec{J} = i\omega\vec{P}$ ) through refractive index perturbations  $\Delta n(\vec{r})$ .  $\Delta\epsilon(\vec{r})$  is the dielectric permittivity perturbations,  $\epsilon_o$  is the vacuum permittivity, and  $n$  is the average dielectric refractive index. It is assumed that incident light is single frequency (harmonic time dependence). The fractional amplitude,  $A_n$ , of the propagating mode that scatters into the same spatial mode, but propagating in the backward direction, can be determined using the approach described in ref [47] and is given by the following expression,

$$A_n = \frac{-\int_V \vec{J} \cdot \vec{E}_n^* dV}{2 \int_S \vec{E}_n \cdot \vec{H}_n^* dS} = \frac{-i\omega \int_V \Delta n(\vec{r}) |\vec{E}_n(\vec{r})|^2 dV}{c \int_{\text{all}} |\vec{E}_n(\vec{r})|^2 dS} \quad (9)$$

where  $\vec{H}_n$  is the magnetic field,  $V$  is the scattering volume (taper volume) such that the volume differential  $dV$  can be expressed as  $dV = dS dz$  where  $dS$  is the differential cross-sectional area and  $dz$  is the differential length along the taper axis. In addition, “all” indicates integration over the infinite cross sectional area.

The fraction of the scattered power that couples into the backward guided mode is the ensemble average of the magnitude-squared of Eq. (9). If  $P_{\text{in}}$  and  $P_s$  are the input power (assumed constant along the taper) and the backscattered power that is coupled into the guided taper mode, then they are accordingly related by,

$$P_s = \frac{\omega^2 \int_{V'} \int_V |\vec{E}_n(\vec{r})|^2 \langle \Delta n(\vec{r}) \Delta n(\vec{r}') \rangle |\vec{E}_n(\vec{r}')|^2 dV dV'}{c^2 \left( \int_{\text{all}} |\vec{E}_n(\vec{r})|^2 dS \right) \left( \int_{\text{all}} |\vec{E}_n(\vec{r}')|^2 dS' \right)} P_{\text{in}} \quad (10)$$

The correlation length of the scattering centers is assumed to be much smaller than the scale of the wavelength. The correlation function of the refractive index fluctuation is therefore taken as proportional to a delta-function,

$$\langle \Delta n(\vec{r}) \Delta n(\vec{r}') \rangle \equiv \langle \Delta n^2 \rangle V_c \delta(\vec{r} - \vec{r}') \quad (11)$$

where  $V_c$  is the scattering volume [47]. This delta-function correlation eliminates one of the volume integrations in Eq. (10). Next, by introducing the infinitesimal power  $dP_s(z)$  that is scattered from the volume with infinitesimal thickness,  $dz$ , the following equation results from Eq. (10) after simplification using Eq. (11),

$$dP_s(z) = \frac{\omega^2 \langle \Delta n^2 \rangle V_c \int_S |\vec{E}_n(\vec{r})|^4 dS}{c^2 \left( \int_{\text{all}} |\vec{E}_n(\vec{r})|^2 dS \right)^2} P_{\text{in}} dz \quad (12)$$

In a statistically homogeneous scattering medium, the Rayleigh scattering coefficient,  $\alpha$ , can be related to the refractive index fluctuation  $\langle \Delta n^2 \rangle$  and average refractive index  $n$  [52] as follows,

$$\alpha = \frac{32\pi^3 n^2}{3\lambda^4} \langle \Delta n^2 \rangle V_c \quad (13)$$

Upon substitution in Eq. (12) this gives the result,

$$\frac{1}{P_{\text{in}}} \frac{dP_s(z)}{dz} = \frac{3\lambda^2}{8\pi n^2} \alpha \frac{\int_S |\vec{E}_n(\vec{r})|^4 dS}{\left( \int_{\text{all}} |\vec{E}_n(\vec{r})|^2 dS \right)^2} \quad (14)$$

By assuming there are distinct scattering regions (i.e., core, cladding, surface) with their own corresponding Rayleigh coefficients ( $\alpha_i$ ,  $i \in \{\text{core, clad, ss}\}$ ), we replace the above single region result by a summation over the regional scattering contributions.

$$\frac{1}{P_{\text{in}}} \frac{dP_s(z)}{dz} = \frac{3\lambda^2}{8\pi n^2} \sum_i \alpha_i \frac{\int_{S_i} |\vec{E}_n(\vec{r})|^4 dS}{\left(\int_{\text{all}} |\vec{E}_n(\vec{r})|^2 dS\right)^2} \equiv \sum_i \alpha_i \sigma_i \quad (15)$$

As an aside, it is a peculiar coincidence that the field integrals involved in  $\sigma_i$  bear a similarity to the effective area in nonlinear optics [60] despite the very different physical contexts. The surface scattering is assumed to be confined to within a small (compared to the wavelength) uniform thickness ( $\Delta t$ ) such that a Rayleigh surface scattering coefficient ( $\beta$ ) can be defined from the Rayleigh scattering coefficient within this surface volume ( $\alpha_{\text{ss}}$ ),

$$\frac{3\lambda^2}{8\pi n^2} \alpha_{\text{ss}} \frac{\int_{\text{ss}} |\vec{E}_n(\vec{r})|^4 dS}{\left(\int_{\text{all}} |\vec{E}_n(\vec{r})|^2 dS\right)^2} = \frac{3\lambda^2}{8\pi n^2} \alpha_{\text{ss}} \Delta t \frac{\oint_{\text{interface}} |\vec{E}_n(\vec{r})|^4 dl}{\left(\int_{\text{all}} |\vec{E}_n(\vec{r})|^2 dS\right)^2} \equiv \beta \eta \quad (16)$$

where,

$$\beta \equiv \alpha_{\text{ss}} \Delta t \quad (17)$$

## Funding

Defense Advanced Research Projects Agency (DARPA) (W31P4Q-14-1-0001, 70NANB11H130); National Science Foundation (NSF) (1125565).

## Acknowledgments

We thank Dr. Hsieh-Chen Tsai and Dr. Albert Chern at Caltech for their helpful discussions and comments on this work.